Materials Today Communications 25 (2020) 101591

Contents lists available at ScienceDirect

Materials Today Communications

journal homepage: www.elsevier.com/locate/mtcomm

Effect of friction stir welding (FSW) on the electrochemical behavior and galvanic coupling of AA2024-T3 and AA7475-T651

A.F.S. Bugarin[a,*], C.P De Abreu[a], M. Terada[b], H.G. De Melo[c], I. Costa[a]

[a] Instituto de Pesquisas Energéticas e Nucleares, Centro de Ciência e Tecnologia de Materiais, Av. Prof. Lineu Prestes, 2242, São Paulo, SP, 05508-000, Brazil
[b] Instituto SENAI de Inovação em Manufatura Avançada e Microfabricação, Rua Bento Branco de Andrade Filho, 379, São Paulo, SP, 04757-000, Brazil
[c] Universidade de São Paulo, Depto. Engenharia Metalúrgica e de Materiais, Av. Professor Mello Moraes, 2463, São Paulo, SP, 05508-030, Brazil

ARTICLE INFO

Keywords:
Friction stir welding
FSW
Dissimilar alloys
AA2024
AA7475
Corrosion resistance

ABSTRACT

In this study, the local electrochemical activity of AA2024-T3 and AA7475-T761 joined by friction stir welding (FSW) was investigated as a function of time by electrochemical tests in 0.01 mol L^{-1} NaCl solution using a mini cell. The welding procedure resulted in increased electrochemical activity of the weld affected zones of both alloys, which electrochemical activities increased with immersion time, as demonstrated by the electrochemical behavior. In the heat affected zone (HAZ) and the thermomechanically affected zone (TMAZ) of AA7475-T651 the increased activity was due to precipitation of η phase at the grain boundaries stimulated by thermo-mechanical effects. On the other hand, the enhanced activity in the TMAZ/HAZ of the AA2024-T3 was associated to a large concentration of copper rich cathodic particles broken by tool rotation that were spread along this zone. However, the zone of highest electrochemical activity was the stir zone (SZ) and this was ascribed to galvanic coupling between the two alloys, AA2024-T3 and the AA7475-T651, where the former acted as cathodic and the latter as anodic area.

1. Introduction

High strength aluminum alloys show excellent combination of mechanical and physical properties and consequently are widely used in aeronautic, architecture, transport industriesand also in others sectors requiring improved mechanical properties [1]. Large Al panels must be assembled to achieve the final shape property, when used in huge structures like aircrafts. For instance, aluminum alloys of the 2XXX and 7XXX series are used in the wing structure [2–5]. However, joining these alloys by conventional fusion weld methods generates defects in the joints, such as cracking, residual stresses and porosities [6–8]. Therefore, panels are frequently joined using rivets, increasing the final weight of the structure.

In 1991, the Welding Institute (TWI) developed the friction stir welding (FSW) process, a solid-state joining method performed at temperatures below the materials melting point [6–9]. This process uses a non-consumable rotating tool, employs lower heat input and does not require metal addition or gas protection [10–12], avoiding some of the welding problems previously mentioned. Besides providing joints with better characteristics (less defects, low distortion and improved joints performance) [13]. One of the main FSW achievements for large Al-based structures used in the aerospace industry is weight reduction due to rivet elimination [13,14]. Indeed, as documented in technical information released by digital platforms, each Airbus A380 wing contains 750.000 rivets [15], whereas the assembly of a Boeing 747–8 has 1,000,000 of them [16]. Although it can be considered a relatively new joining technique, FSW is already being used in the aerospace industry for fabricating large volume fuel tanks for different space programs [13] as well as commercial aircrafts, like the executive jet Eclipse 500, which had 263 parts joined by FSW, representing the substitution of more than 7300 fixation elements (approximately 60 %) [6], effectively contributing for weight reduction and, therefore, lowering fuel consumption, which are considered two of the main goals of the modern aircraft industry [17].

Despite its advantages, FSW causes microstructural changes in the weld affected zones, either due to heating or to mechanical effects or even by the combined action of them. Four different zones with varied microstructure result from FSW, namely: unaffected base metal (BM), heat affected zone (HAZ), thermomechanically affected zone (TMAZ) and stir zone (SZ) [6,14,18,19].

Due to the increased technological interest, in the last decades, in the FSW process, a number of works were published aiming to investigate the microstructure, mechanical properties and the corrosion behavior of FSWed aluminum alloys, most of them using similar alloys

* Corresponding author.
E-mail address: afbugarin@usp.br (A.F.S. Bugarin).

https://doi.org/10.1016/j.mtcomm.2020.101591
Received 27 April 2020; Received in revised form 3 August 2020; Accepted 13 August 2020
Available online 01 September 2020

Table 1
Chemical compositions (wt. %) of the aluminum alloys.

Element	Al	Mg	Cu	Zn	Si	P	S	Ca	Ti	Cr	Mn	Fe
2024	92.3	1.60	4.80	0.08	0.19	0.03	0.02	0.04	0.05	0.04	0.64	0.22
7475	89.4	1.90	1.70	6.20	0.15	0.03	0.05	0.06	0.04	0.22	0.02	0.12

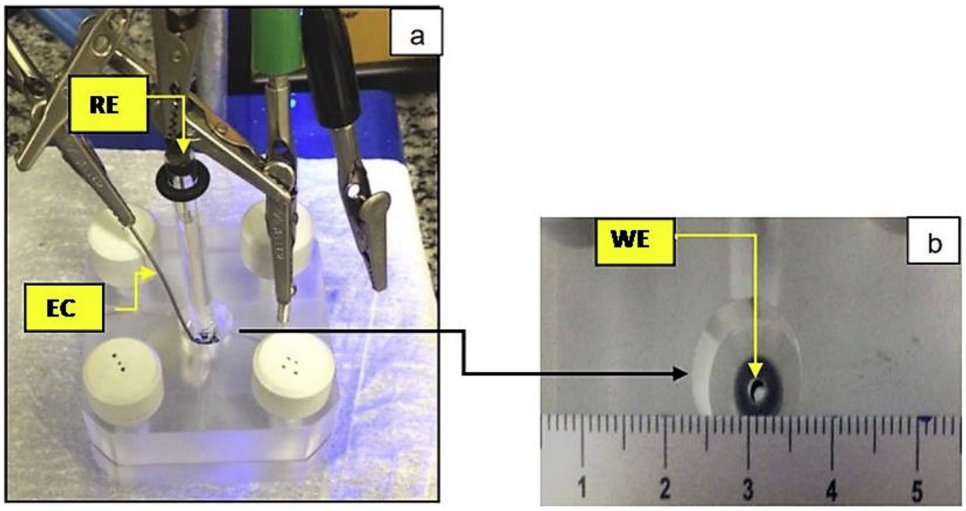

Fig. 1. The mini cell with exposed area of 0.035 cm^2 in a three-electrode setup configuration used in corrosion tests.

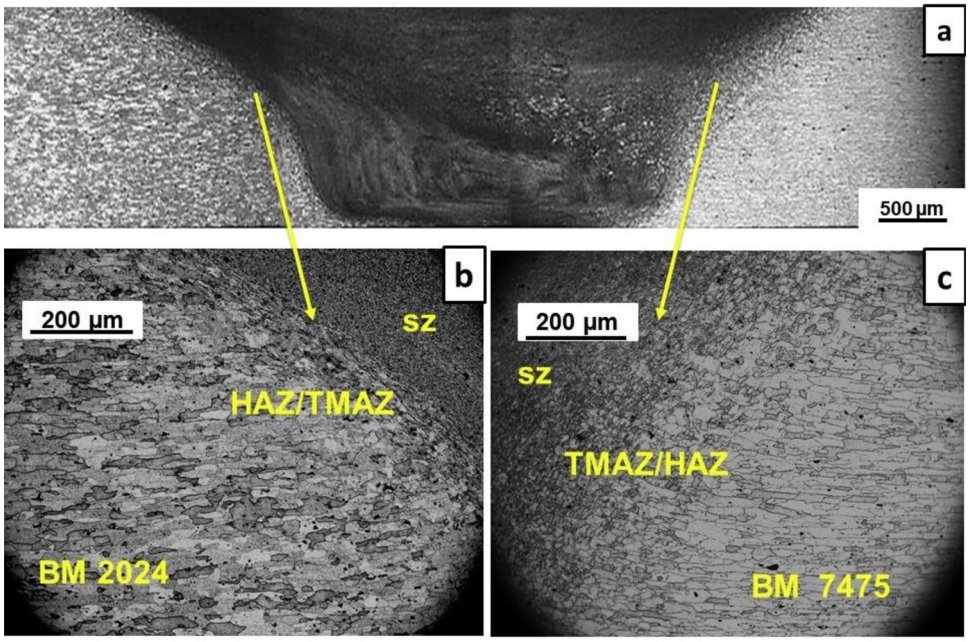

Fig. 2. (a) Grain structure on transverse cross-section of dissimilar FSW between AA2024 and AA7475 and higher magnification of (b) advancing and (c) retreating sides after etching with a solution of 25 ml HNO_3 and 2 ml HF in 100 ml H_2O.

as substrates. Concerning the studies about the corrosion behavior of FSWed similar 2XXX or 7XXX Al panels, it is frequently reported that the most susceptible regions to corrosion are found within the weld affected zone [20–25], even though some works indicate improved corrosion resistance for this zone, particular for Al-Cu-Li alloys [26,27].

Complex structures like aircrafts, frequently establishes a main desired property for structural components. For instance, for the upper wing-stringer the static material properties that influence the design are compressive yield strength and modulus of elasticity in compression, on the other hand, for the lower skin-stringer the desired static properties are: tensile strength, tensile yield strength and tensile modulus [17]. This occurs because the former structure is in compression during flight, whereas the latter is primarily in tension [17]. Therefore, different alloys brands must be used either for different structural components or even in the same component, depending on the specific structural and load requirements. In aircrafts, different aluminum alloys of the same or different brands can be joined [28]. In the literature, only few works were devoted to investigating the corrosion behavior of dissimilar Al alloys welded by FSW. For alloys not used in the aerospace industryis reported higher corrosion resistance of the welded joint

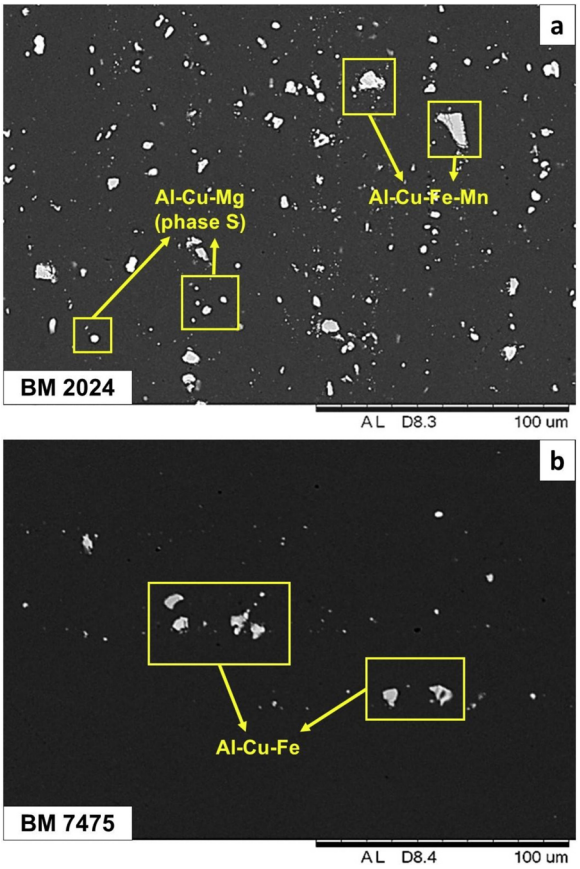

Fig. 3. SEM micrographs after polishing of the BM of (a) AA2024-T3 and (b) AA7475-T651.

when compared with the base metals [8,29]. Patil and Soman [29] also report that the corrosion current of the welded (6082/6061) joint decreased with the tool travel speed when alloy 6082 was positioned at the advancing side and increased when the 6061 was at this position [29]. Davoodi et al. [30] found that the corrosion of the FSW joint between AA5083 (non-aerospace) and 7023 (aerospace) alloys takes place at the interface between both materials, denominated by the authors as "borderline". According to the authors, the difference in hardness between the two materials could explain this difference [30].

Concerning works specifically devoted to investigating the corrosion behavior of FSWed 2XXX and 7XXX alloys, all the results show that the corrosion process is mostly concentrated in the 7XXX material [4,12,31]. For an Al–Li–Cu alloy and Al–Zn–Mg–Cu alloy joint, Wu et al. [31] found that the HAZ of the 7XXX alloy, placed at the AS, was the most susceptible zone to the exfoliation corrosion susceptibility test (EXCO), likely due to a wide precipitate free zone (PFZ) and the precipitation of coarse η phase at the grain boundaries. This zone also presented the lowest open circuit potential (OCP) values, indicating that it can be galvanically sacrificed.

Niu et al. [2], in tests on dissimilar joints in EXCO solution, the authors verified the difference in OCP when positioning the AA2024 on AS and the AA7075 on the RS, compared with the AA2024 alloy on RS and AA7075 on the AS. The authors observed that the location of the MB in the AS or RS affects the corrosive performance of the SZs.

The OCP values of SZ with the AA2024 in the AS showed higher values. Moreover, they also noted that the OCP of SZ was similar to the OCP of the MB that was located in RS in both cases. However, through the electrochemical corrosion tests of the 2A12/7075 dissimilar FSW joint, Zhang et al. [32] observed that the corrosion resistance of SZ was better when of the AA7075 was positioned at the AS. The authors were also observed positive results in intergranular corrosion resistance of the SZ when AA7075 was at the AS. The intergranular corrosion resistance of the SZ exhibited was better than BM. The location of the material in the advancing side (AS) or retreating side (RS), as an effect on the electrochemical activity even with similar alloys, as investigated by Queiroz et al. [33] with AA2024. The authors observed that clusters of coarse intermetallic particles were more abundant in the TMAZ of the RS, and this resulted in the formation of more severe localized corrosion (SLC) sites in this region. Zhang et al. [34] in studies with FSWed AA2024 and AA7075 joints observed that the rotation speed mainly affects the local microstructure and the corrosion resistance of the analyzed joints. In the polarization tests, SZ showed a higher corrosion current density due to the occurrence of galvanic corrosion.

Galvanic coupling effects were also verified by Sidane et al. [12] and de Abreu and collaborations [4] for 2XXX-7XXX FSWed plates. In both investigations, the welded joint OCP was intermediary to that of the 2XXX (higher) and 7XXX (lower), indicating, respectively, cathodic and anodic polarization. Galvanic coupling was demonstrated in the work of de Abreu et al. [4] by means of Local Electrochemical Impedance Spectroscopy (LEIS), whereas SEM image presented by Sidane et al. [12] showed localized corrosion of the 7449 alloy at the weld center line, near the interface with the 2050 alloy.

In the studies involving FSWed 7XXX-2XXX alloys, except in the work of Wu et al. [31], where OCP measurements seem to be performed isolating each different zone of the weld, the electrochemical measurements were carried out using the whole welded piece (comprising the whole welded zone). None of them report results on the electrochemical behavior of the individual (non-coupled) zones. Therefore, multiple galvanic coupling effects are reported in the experimental results and, often, only the zone most susceptible to corrosion can be identified. In the present work a microcell was employed to access the electrochemical behavior in 0.01 mol L^{-1} NaCl solution of the different zones affected by welding of AA2024-T3 and AA7475-T761 joined by FSW. The EIS behavior was followed with immersion time and the individual corrosion susceptibility ranked and associated with microstructural features.

2. Materials and methods

The materials used in this study were AA2024-T3 and AA7475-T761. The chemical compositions of both alloys were determined by X-ray fluorescence spectroscopy and are presented in Table 1. The alloys were produced by ALCOA and provided by Embraer as friction stir welded sheets, with 2 mm thickness. The FSW process was carried out with the tool rotating clockwise with the AA2024 at the advancing side (AS), and the AA7475 at the retreating side (RS) of the welded joint. AA2024 application in AS was due to its less hardness [35].

For microstructural and electrochemical characterization, the samples were grounded with SiC emery paper up to #4000 and then polished with diamond paste up to 1 μm. Subsequently, they were

Table 2
Chemical composition (wt. %) of the constituent particles dos MB of both alloys.

		Al	Cu	Mg	Fe	Mn	Zn
2024	S – phase	637 ± 3.7	29.2 ± 1.0	7.1 ± 3.5	–	–	–
	Al-Cu-Fe-Mn	68.7 ± 2.6	16.1 ± 2.6	–	9.1 ± 0.8	5.7 ± 0.4	–
7475	Al-Cu-Fe-Zn	72.2 ± 1.8	7.5 ± 1.9	–	16.8 ± 2.3	–	3.5 ± 0.5

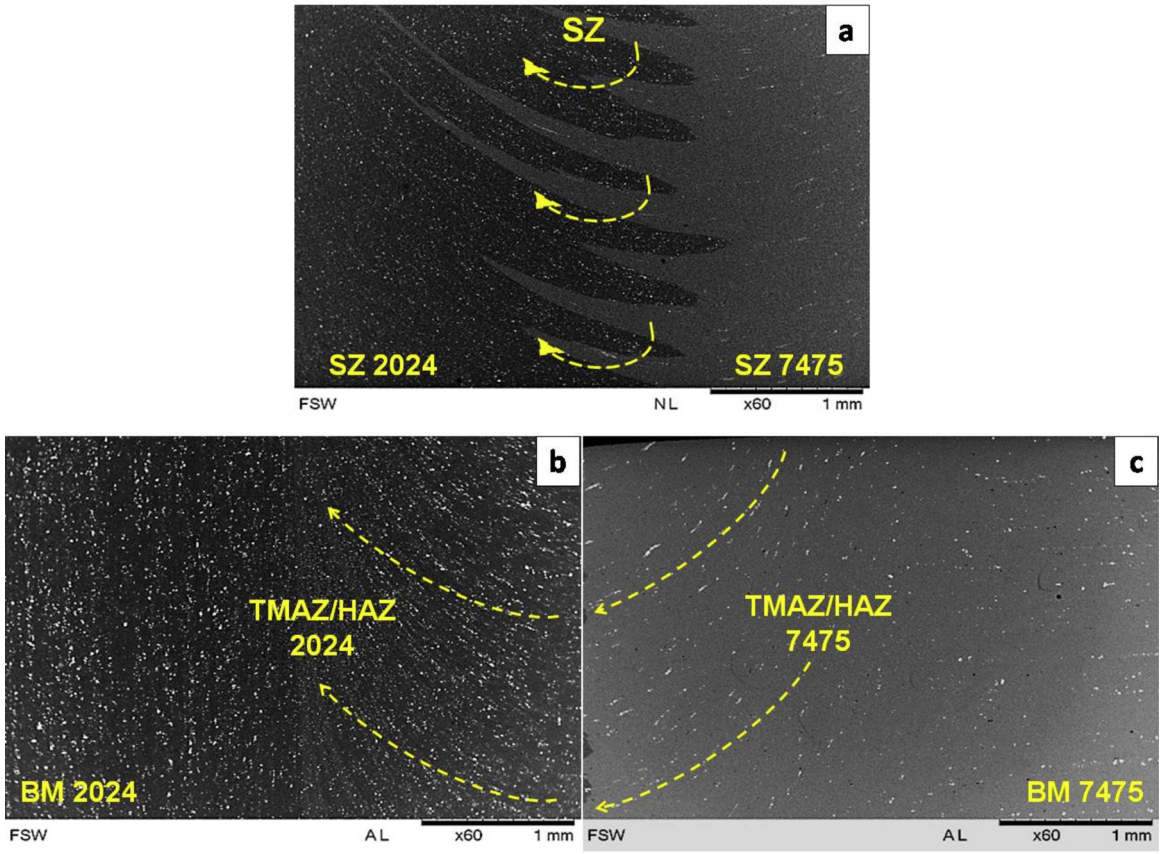

Fig. 4. SEM micrographs of (a) SZ; (b) TMAZ, HAZ and BM of AA2024; (c) TMAZ, HAZ and BM of AA7475. Arrows indicate the direction of rotation of the welding tool.

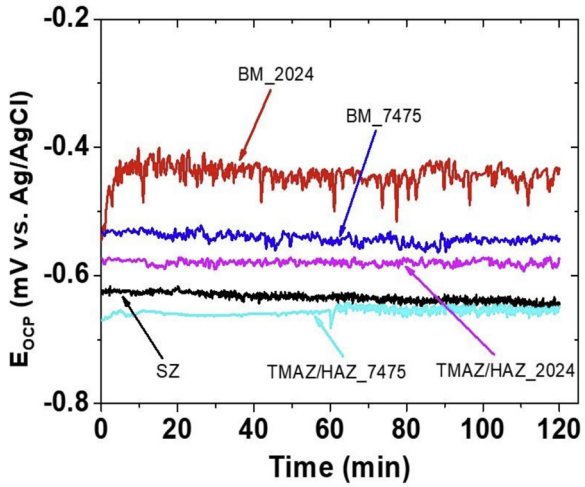

Fig. 5. Open circuit potential variation with exposure timeof the various zones in the AA2024 and AA7475 alloys welded by FSW and exposed to 0.01 mol L^{-1} NaCl solution.

degreased with 99.5 % ethanol, washed with distilled water and dried under a hot air stream. The samples for transmission electron microscopy (TEM) analysis were used as discs of 3 mm diameters. The samples were grounded with SiC emery paper #1200 up to thick of about 100 μm. After done that, electrolytic etching was performed in a solution composed of 20 % nitric acid in methanol at 25 V and at −30 °C using a TenuPol equipment. The imaging was carried out using a JEOL 2100 microscope, operanting in 200 kV.

Etched samples of the transverse cross-section (25 ml HNO3 and 2 ml HF in 100 ml H2O at (4 ± 1) °C [36]) were also prepared to reveal the grains structures of the base metal and of the different weld zones. Etching was performed by gently swabbing the sample surface with cotton soaked with the etchant.

The electrochemical behavior was analysed on the surface of sample of the different weld zones and of the two base metals (BM). It was initially monitored by open circuit potential (OCP) measurements and subsequently by electrochemical impedance spectroscopy (EIS). A mini cell (exposed area of 0.035 cm^2), Fig. 1, in a three-electrode setup configuration was used, with an Ag/AgCl/KCl_{Sat} as the reference electrode, a platinum wire as the auxiliary electrode and the working electrode corresponding to the tested zone. The volume of electrolyte used in the mini cell was 50 mL. Potentiodynamic polarization curves were also obtained after 2 h of immersion; with a scan rate of 1 mV/s. Electrochemical measurements were performed in the electrolyte composed of naturally aerated 0.01 mol L^{-1} NaCl solution at (22 ± 2) °C. EIS measurements were carried out from 5 h to 24 h of immersion in the electrolyte with signal amplitude of 20 mVrms in the frequency range from 100 kHz to 10 mHz. OCP measuments, EIS tests and potentiodynamic polarization curves were performed in Solartron 1287 potentiostat coupled to a frequency response analyser (FRA). The electrochemical tests were performed in triplicate to check reproducibility

Microstructure and corrosion evolution of the FSW affected zones and of the BM were investigated by using a Leica DMLM optical microscope (OM) and TM3000 Scanning Electron Microscopy (SEM) coupled with energy dispersive X-ray spectroscopy (EDS) detector.

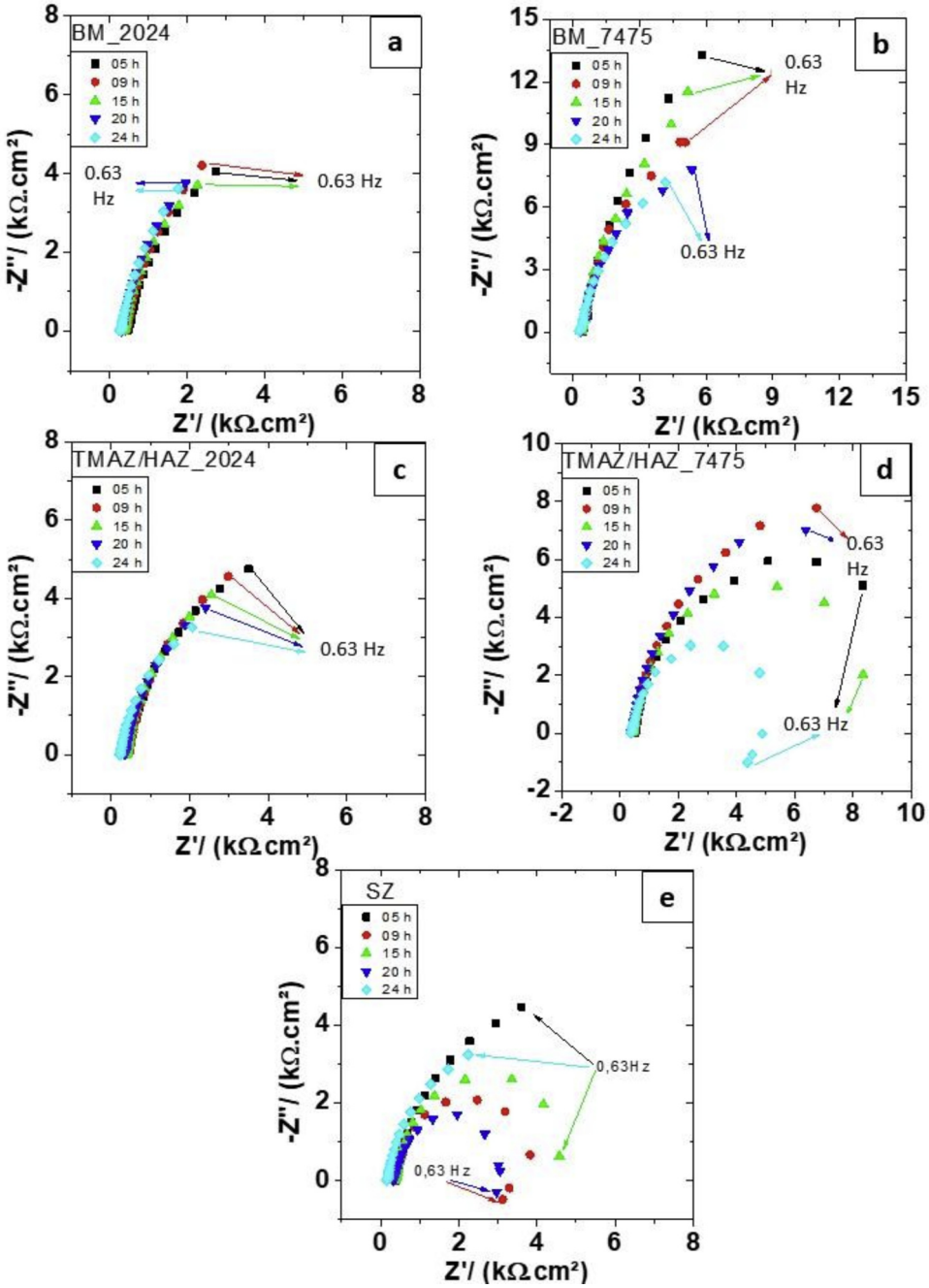

Fig. 6. Nyquist diagrams for various exposure times to 0.01 mol L^{-1} NaCl solution of the (a) AA2024 (b) AA7475, (c) TMAZ of AA2024, (d) TMAZ of AA7475 and (e) SZ.

3. Results and discussion

3.1. Microstructural characterization

The grains structures of the transverse cross-section after metallographic etching are shown in Fig. 2(a–c). The contribution of both alloys is observed by differences in their colors, especially in the underside, Fig. 2(a). The dark zones correspond to the AA2024, and the light to the AA7475, respectively. As reported by other authors [4,5,8,37], significant effects of the FSW on the alloys microstructures, such as modification in the grain sizes and material mixture, were observed.

The SZ observed in Fig. 2(b and c) indicates small and equiaxed grains resulting from dynamic recrystallization due to the FSW process [6]. There is a transition between the elongated grains in the TMAZ/HAZ and the equiaxed grains of the SZ, not only at the advancing side (AA2024), Fig. 2(b), but also at the retreating ones (AA7475), Fig. 2(c). Despite the metallographic attack, it was not possible to determine the extension of the HAZ in both alloys, AA2024 and AA7475), as their grain structures were very similar to their respective base metals. The BM grains of both alloys, without the interference of the FSW process, are elongated and characteristic of rolled materials, Fig. 2(b and c).

The microstructures of both alloys AA2024 and AA7475, observed by Scanning Electron Microscopy (SEM), are shown in Fig. 3(a and b). A comparison of both micrographs shows that the AA7475 is “cleaner” comparatively to the AA2024. A large number of constituent particles were seen in the AA2024, consisting mainly of two types: small round shaped particles, S-phase (Al-Cu-Mg) and particles with irregular shape, mainly Al-Cu-Fe-Mn, according to EDS analysis shown in Table 2

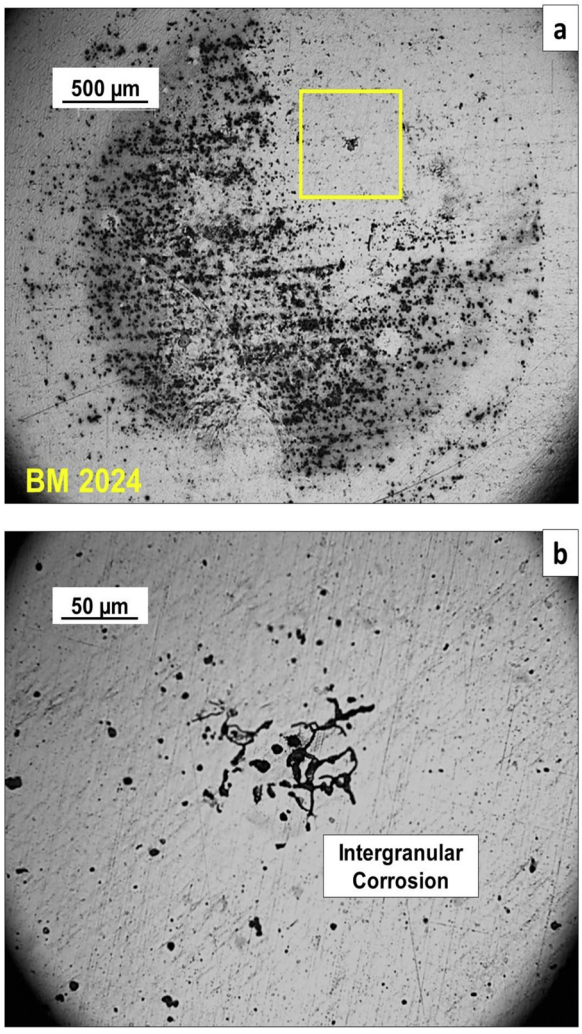

Fig. 7. Optical micrographs of the (a) AA2024 and (b) higher magnification of the corroded area, indicating intergranular and pitting corrosion after 24 h of exposure to 0.01 mol L^{-1} NaCl solution.

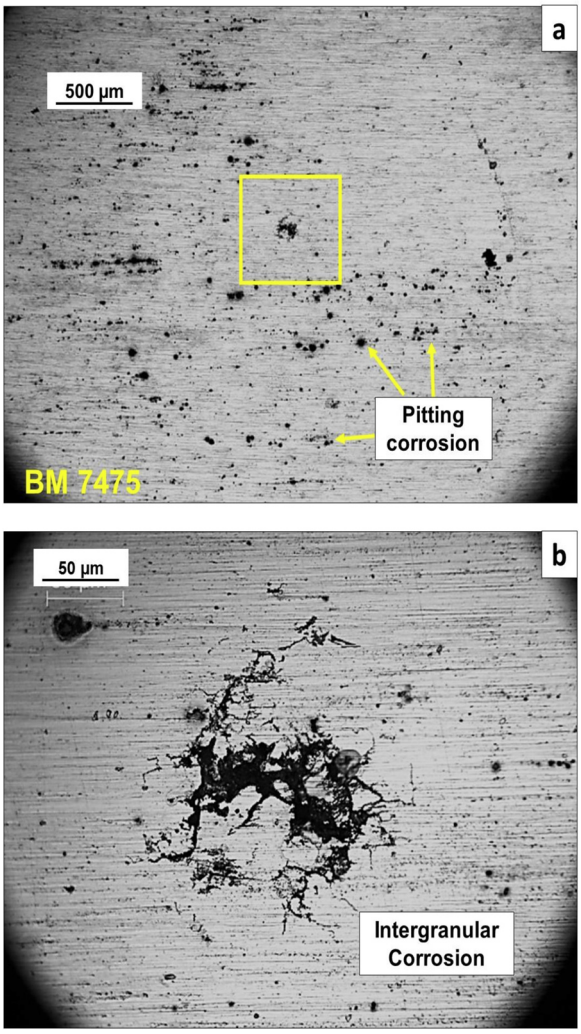

Fig. 8. Optical micrographs of the (a) AA7475 and (b) higher magnification of the corroded area, showing intergranular corrosion after 24 h of exposure to 0.01 mol L^{-1} NaCl solution.

respectively. Fewer particles were seen in the AA7475 compared to the AA2024, and these showed irregular morphologies and diameters up to 10 µm. EDS analysis, Table 2, of these particles showed that these are mainly composed of Al, Cu and Fe [38].

The surface of the welded alloys was observed by SEM and the micrographs of the different zones are shown in Fig. 4(a–c). In the SZ, both alloys tend to mix with each other and there is an extensive interface between them exposed to the electrolyte. The dark areas (left side – Fig. 4(a)) correspond to the AA2024, while the lighter areas (right side – Fig. 4(a)) to the AA7475. The constituent particles are aligned according to the flow of the welding tool rotation, either in the SZ or in the TMAZ, according to arrows indicating the direction of rotation. The microstructures of the HAZ are similar to their BM, either for AA2024 or AA7475, as shown in Fig. 4(b) and (c), respectively, and, as already reported by OM characterization of the etched sample, it was not possible to establish the width of the HAZ by microscopic analysis. Thereby, in this study, the electrochemical characterization was carried out in the SZ, TMAZ/HAZ and the BM of both alloys.

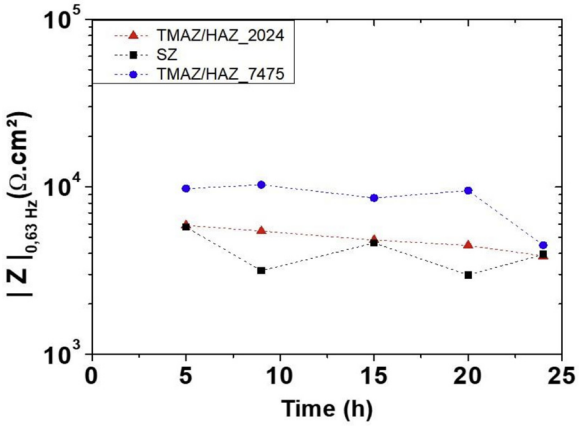

Fig. 9. Variation of |Z|0.63 Hz as a function time for SZ and TMAZ/HAZ of the AA2024 and AA7475 in 0.01 mol L^{-1}NaCl solution.

3.2. Electrochemical characterization

Open circuit potential (OCP) measurements obtained with a mini cell for the various welded alloys zones, as a function of exposure time in the 0.01 mol L^{-1} NaCl solution, are presented in Fig. 5. The OCP of the BM of AA2024 showed large oscillations, indicating high electrochemical instability in this alloy. This is due to its high number of constituent particles, as shown in Fig. 3(a), which promotes the onset of localized corrosion, after short immersion times [39–42]. In the BM of AA7475, oscillations also occurred along the period of testbut with

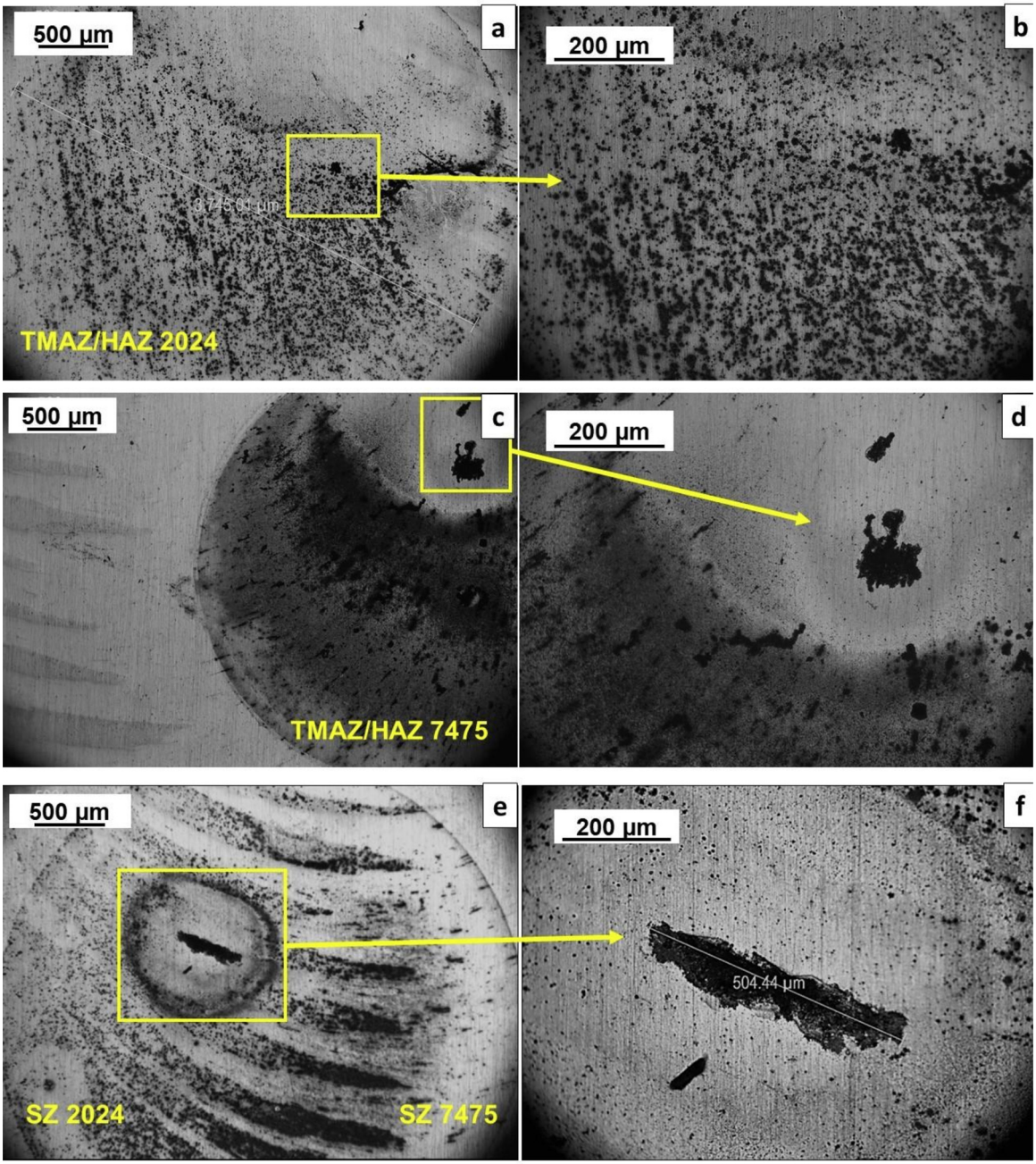

Fig. 10. Optical micrographs of the (a-b) HAZ/TMAZ of the AA2024, (c-d) TMAZ/HAZ of the AA7475 (e and f) SZ after 24 h exposure to 0.01 mol L^{-1} NaCl solution.

lower frequency and smaller amplitudes.

The zones affected by FSW (TMAZ/HAZ and the SZ) presented more negative OCP compared to their corresponding BM showing that the effects of FSW on the alloy microstructure are substantial and can be detected by this simple procedure. Intermediate OCP values, between that of TMAZ/HAZ, was measured in the SZ of the two alloys, indicating that galvanic coupling effects might occur. However, the OCP of the SZ was closer to that of the TMAZ/HAZ of the AA7475. Concerning the BM, lower OCP was related to the AA7475 (Zn-rich) comparatively to the AA2024 (Cu-rich). However, it is important to notice that direct galvanic coupling between the two BM does not occur as they are not directly coupled, even though cathodic and anodic polarization effects might be expected when both BM and the weld zones are exposed together to an aggressive media. Interestingly, the relative OCP values presented in this study are not in accordance with those reported by de Abreu et al. [4] for the same alloys welded by FSW, but in a different solution (0.1 mol L^{-1} Na_2SO_4 + 0.001 mol L^{-1} NaCl). These authors used a macro cell to analyze the joint and reported an intermediate value for the OCP of the welded sample in comparison with the respective BM (OCP AA2024 > OCP joint > OCP AA7475). However, the authors observed that the EIS results of the FSW joint showed lower corrosion resistance than the BM of both alloys. In this study, the difference is explained by the microstructure modifications induced by the welding process carried out to develop localized corrosion more intense at the TMAZ/HAZ at the AA7475 side of the weld. The use of the mini cell allowed to restrict the area analysed to different zones resulting from FSW, whereas the macro cell exposes a mixture of zones not being possible to separate the specific contribution of one zone and its microstructure to the electrochemical behavior. Besides sulphate and chlorides ions compete for the same surface also affecting the electrochemical results. The literature reports the effects of sulphate ions in sodium chloride solutions on pure aluminium [43]. It is suggested that

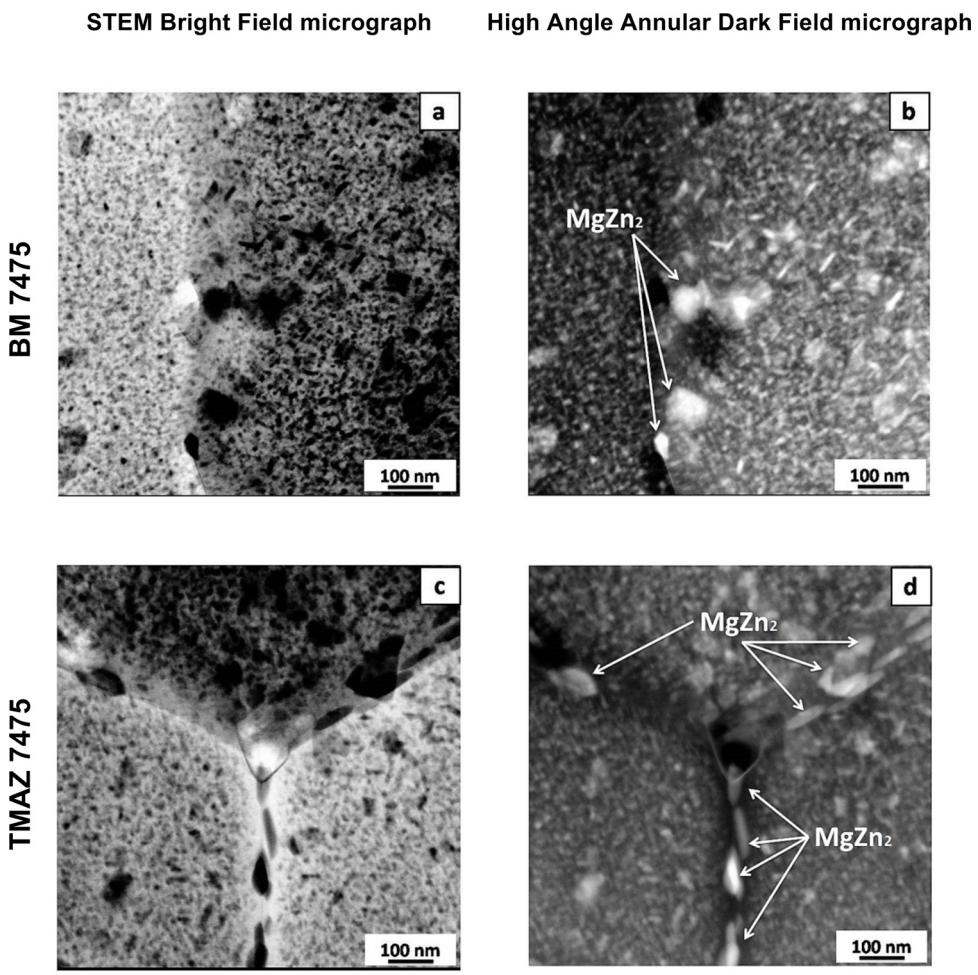

Fig. 11. Bright Field and High Angle Annular Dark Field Transmission Electron Micrographs of (a and b) BM of the AA7475 and (c and d) TMAZ/HAZ of the AA7475.

SO_4^{-2} ions retard the oxide film breakdown by Cl- ion incorporation into the film.

In this study, the evolution of the electrochemical behavior of each individual region was monitored by EIS using the mini cell, and the results are presented in Fig. 6(a–e). Data dispersion was seen in the lower frequency region. Consequently, only the results obtained at higher and medium frequencies are presented.

A comparison of both aluminum alloys (BM) shows lower impedance values for the AA2024 compared to the AA7475. This is in accordance with the OCP results interpretation and can be ascribed to the more complex microstructure of the former alloy when compared to the latter. The low magnification OM images acquired after 24 h exposure to the electrolyte, displayed in Figs. 7(a and b) and 8 (a and b), clearly demonstrate the difference in electrochemical activities. They show a large proportion of the exposed surface of the AA2024 with visible localized corrosion sites, whereas for the AA7475, corrosion sites are dispersed in the surface.

EDS analysis of the corrosion products was performed after 5 h of immersion test. Corrosion products composed of Al, O, Zn, Fe, Cu and Cl were found in large amounts on the AA7475, covering the entire surface. The amount of corrosion products found on the AA2024 was concentrated mainly on the precipitates and these were composed of Al-Cu-O (data not shown). It was not possible to perform EDS analysis for long immersion times, due to the great amount of corrosion products on the surface.

For the AA2024, the impedance varied along the period of test (Fig. 6 (a)). This can be attributed to the activation and deactivation of corrosion sites, with deactivation occurring not only due to the detachment of corroded IM particles but also due to their partial or total coverage by corrosion products. For this alloy, the selective attack of the initially anodic Mg-rich IM (S-phase) leads to copper enrichment reversing its polarization. Reduction of oxygen on these particles leads to alkalization at their surroundings, with the consequent cathodic attack of the aluminum oxide film [39].

In the case of the AA7475, despite its higher impedance comparatively to the AA2024, there was a steady decreasing trend of the impedance modulus (Fig. 6 (b)). After 24 h of test, the surface of this alloy showed both, pitting (Fig. 8 (a)) and intergranular corrosion (Fig. 8 (b)). However, as previously stated, fewer areas were affected by corrosion in comparison with the AA2024.

EIS results for the TMAZ/HAZ of both alloys showed lower impedance values when compared to their respective BM. For the TMAZ/HAZ of AA7475 (Fig. 6 (d)), there was a large decrease in impedance modulus with time, and after 24 h of test, an inductive loop was seen at the low frequencies, as also observed for SZ (Fig. 5 (e)). The presence of inductive loops at low frequencies for aluminum alloys is typical of strong localized attack [44].

In the Fig. 9 compares the impedance modulus of the welded affected zones at 0.63 Hz. The corrosion resistance increased in the following order: SZ < TMAZ/HAZ (AA2024) < TMAZ/HAZ (AA7475). The lowest impedances related to the SZ is caused by galvanic coupling of the two alloys and the high electrochemical activity of the TMAZ in both alloys, AA2024 and AA7475, which are the zones of the two alloys in contact with each other. The SZ impedance values were close to those of the TMAZ/HAZ of the AA2024, suggesting that the contribution of this alloy in the galvanic coupling related to the SZ predominated over

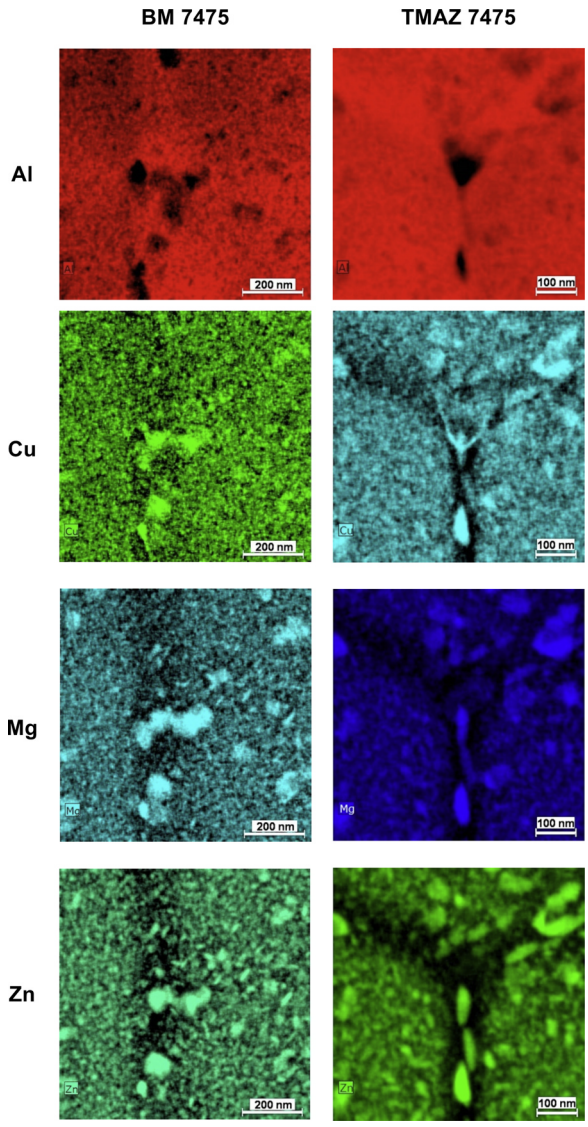

Fig. 12. HAADF-STEM micrographs of precipitates found in BM and TMAZ in AA7475.

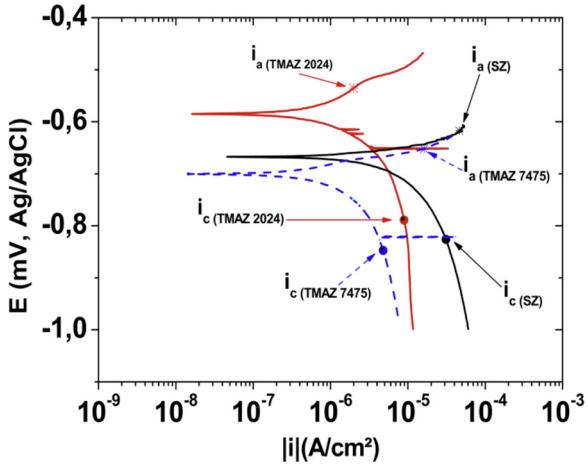

Fig. 13. Potentiodynamic polarization curves of the TMAZ/HAZ AA2024, AA7475 and SZ after 2 h of exposure to the 0.01 mol L^{-1} NaCl solution. Overvoltage of +50 mV (anodic) and −150 mV (cathodic) in relation to the corrosion potential of each zone are indicated.

Table 3
i_a and i_c values obtained from Fig. 13 in the FSW zones after 2 h of exposure to 0.01 mol L^{-1}NaCl solution.

	i_a* (A/cm²)	$\|i_c\|$** (A/cm²)
TMAZ 2024	2.0×10^{-6}	8.8×10^{-6}
SZ	4.8×10^{-5}	3.0×10^{-5}
TMAZ 7475	1.8×10^{-5}	4.8×10^{-6}

* overvoltage of +50 mV in relation to the corrosion potential of each zone.
** overvoltage of −150 mV in relation to the corrosion potential of each zone.

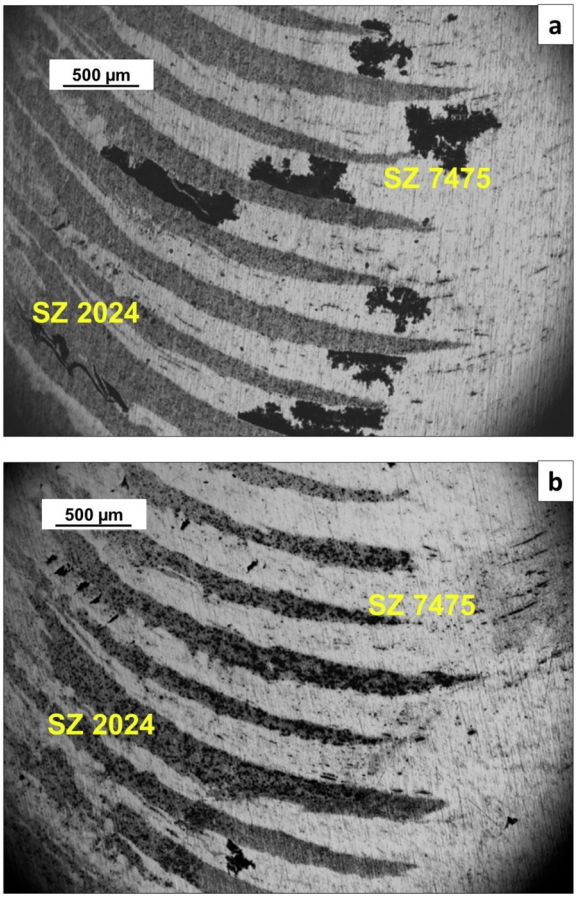

Fig. 14. Optical micrographs of the SZ after (a) anodic and (b) cathodic polarization in a 0.01 mol L^{-1} NaCl solution.

that of the AA7475. This could be associated to the higher electrochemical activity in the TMAZ of the AA2024 comparatively to the AA7475, due to the higher concentration of precipitate particles in the AA2024.

Fig. 10 (a–f) displays the OM of the FSW after 24 h of immersion in the electrolyte. Due to the fact that two different materials were FSWed, the formation of a mixed structure within the SZ is inevitable. Typically, the SZ is characterized by an onion ring structure. Besides, fine particle of the material in the advancing side (AA2024) disperse throughout the stir zone of the retreating material (AA7475). That is the main reason regarding the heterogeneous corrosion resistance in the stir zone. Even though presenting a higher density of corroded areas, the aspect of the TMAZ/HAZ in the AA2024 (Fig. 10(a and b)) is very similar to its BM, associated with the constituent particles. Queiroz et al. [33] showed that clustering of broken constituent particles may enhance local corrosion activity at the TMAZ/HAZ of the AA2024 welded by FSW. Conversely, the SZ of the AA7475 exhibits a region with intense localized attack (Fig. 10 (c) – top right side) that seems to protect its

surroundings. The FSWed process may have favored the precipitation of MgZn2, the main cause of intergranular corrosion in 7XXX alloys.

Fig. 11(a–d) presents TEM micrographs of the BM and the TMAZ/HAZ in the AA7475. They clearly show accumulation of aligned precipitates at the grain boundaries of the TMAZ/HAZ zone. An investigation of microstructural evolution in AA7075 during FSW by Mahoney et al. [45] concluded that maximum process temperatures are between 400 and 480 °C. EDX analyses of these precipitates, Fig. 12, showed that they are composed of Mg and Zn, the main constituents of η phase. This suggests that the solubilization temperature of η phase was reached in the TMAZ during FSW, and solubilization was followed by η phase preferential reprecipitation at the grain boundaries. Abreu and co-workers [4] realized differential scanning calorimetry analyse (DSC) in the AA7475 and proved that η fase dissolution just above 400 °C. Therefore, the η precipitation increased intergranular corrosion activity, as it has been reported in literature [5,31,38,46,47].

Anodic and cathodic potentiodynamic polarization curves corresponding to 2 h immersion in the 0.01 mol L^{-1} NaCl electrolyte are presented in Fig. 13. The values presented refer to the regions where the effect of galvanic coupling was observed, ie TMAZ/HAZ zones of the two BM and SZ. As the corrosion potentials presented significant differences, to allow a better quantitative comparison for each weld zone, anodic (i_a) and cathodic (i_c) current densities were determined at overpotentials of +50 mV and −150 mV, respectively. The results are shown in Table 3. For each branch, the current density was greater at the SZ, confirming the increased electrochemical activity of this zone, as already indicated in the EIS diagrams and in accordance with previous investigation [4]. Concerning the behavior of both TMAZ/HAZ zones, the AA7475 exhibited larger i_a, whereas i_c was greater for the AA2024. The former behavior can be explained by the stronger IGC susceptibility of the TMAZ/HAZ in the AA7475, whereas the increased amount of IM leads to increased the TMAZ/HAZ in the AA2024. Indeed, the OM images of these regions (not presented in the manuscript) confirmed such features.

In the Fig. 14 shows OM micrographs of the SZ after (a) anodic and (b) cathodic polarization tests. After cathodic polarization, it was observed that corrosion occurred mainly at the vicinity of the precipitates in the AA2024 alloy, in accordance with the recognized cathodic role of these precipitates [39–41]. Conversely, anodic polarization resulted in intense corrosion of the AA7475, mainly at the interface between this alloy and the AA2024, which exhibited very few localized corrosion sites.

A corrosion mechanism has been previously proposed for the same welded alloys by Abreu et al. [4]. According to this mechanism, when in contact with the electrolyte, anodic polarization of the AA7475 leads to Zn dissolution from the constituent particles due to its high reactivity and on the AA2024 cathodically polarized, oxygen reduction with hydroxyl ions formation occurs on top of the Cu rich particles in the AA2024 alloy. Also Mg in the AA2024 Cu rich particles is dissolved from these particles. The anodic dissolution of Zn ions followed by their migration to the cathodic regions of AA2024 generates Zn hydroxide. The Zn hydroxide precipitation occurs mainly on the phase-S due to a local pH increase associated to the oxygen reduction reaction. The Mg from the S-phase oxidizes depending on the distance between the SZ and the affected particle, but the S-phase remains active for the oxygen reduction reaction. When the immersion time increases, constituent particles are progressively covered by Zn hydroxides, leading to a significant slowdown of the oxygen reduction reaction and the galvanic activity.

4. Conclusions

The corrosion behavior of dissimilar aluminum alloys (AA2024 and AA7475) joined by friction stir welding (FSW) was investigated by electrochemical techniques in function of time using a mini cell and a 0.01 mol L^{-1} NaCl solution. The increased corrosion activity related to the SZ comparatively to the TMAZ/HAZ of both alloys was ascribed to galvanic coupling between the alloys in this zone. The galvanic coupling effect was confirmed by potentiodynamic polarization curves. The SZ showed corrosion potential between both ZTMA/HAZ.

The current density was higher at the SZ, confirming the increased electrochemical activity of this zone. The AA7475 acts as anode whereas the AA2024, as cathode of the galvanic coupling. Intergranular corrosion was identified on both alloys, but predominated in the TMAZ/HAZ of the AA7475, due to the η (MgZn2) phase which was precipitated preferentially at the grain boundaries of the TMAZ. In the TMAZ/HAZ of the AA2024, clustering of broken intermetallics by FSWed process enhanced the local corrosion activity.

This study concluded that the FSW process causes microstructural and electrochemical changes in the Al alloys due to mechanical deformation and/or temperature effect (TMAZ/HAZ). This was possible using a mini cell that allowed to individually test each of the FSW zones (TMAZ/HAZ and SZ); as these electrochemical changes can only be properly characterized if one zone is isolated from the others. It is important to note that the interface between SZ and BM corresponds to the TMAZ/HAZ, and this zone is the most electrochemically active in comparison with the other FSW zones. These modifications show the importance of isolating the FSW zones not only to evaluate their corrosion resistance but also to compare them with the BM.

Data availability

The raw/processed data required to reproduce these findings cannot be shared at this time as the data also forms part of an ongoing study.

Declaration of Competing Interest

The authors report no declarations of interest.

Acknowledgements

Authors acknowledge CNPq (830615/1999-7 and 426280-2016-4) and FAPESP (Proc. 2013/13235-6) for the financial support to this work. MCs Aline de Fátima Santos Bugarin (Proc. 133557/2015-4) is grateful for their grants awarded.

References

[1] ABAL, Associação Brasileira do Alumínio, (2019) (Accessed September 1, 2019), http://abal.org.br.
[2] P.L. Niu, W.Y. Li, N. Li, Y.X. Xu, D.L. Chen, Exfoliation corrosion of friction stir welded dissimilar 2024-to-7075 aluminum alloys, Mater. Charact. 147 (2019) 93–100, https://doi.org/10.1016/j.matchar.2018.11.002.
[3] N.Z. Khan, A.N. Siddiquee, Z.A. Khan, A.K. Mukhopadhyay, Mechanical and microstructural behavior of friction stir welded similar and dissimilar sheets of AA2219 and AA7475 aluminium alloys, J. Alloys Compd. 695 (2017) 2902–2908, https://doi.org/10.1016/j.jallcom.2016.11.389.
[4] C.P. De Abreu, I. Costa, H.G. De Melo, N. Pébère, B. Tribollet, V. Vivier, Multiscale electrochemical study of welded Al alloys joined by friction stir welding, J. Electrochem. Soc. 164 (2017) C735–C746, https://doi.org/10.1149/2.0391713jes.
[5] M. Jariyaboon, A.J. Davenport, R. Ambat, B.J. Connolly, S.W. Williams, D.A. Price, Corrosion of a dissimilar friction stir weld joining aluminium alloys AA2024 and AA7010, Corros. Eng. Sci. Technol. 41 (2006) 135–142, https://doi.org/10.1007/978-3-319-99441-3_13.
[6] P.L. Threadgill, A.J. Leonard, H.R. Shercliff, P.J. Withers, Friction stir welding of aluminium alloys, Int. Mater. Rev. 54 (2009) 49–93, https://doi.org/10.1179/174328009X411136.
[7] G. Çam, S. Mistikoglu, Recent developments in friction stir welding of al-alloys, J. Mater. Eng. Perform. 23 (2014) 1936–1953, https://doi.org/10.1007/s11665-014-0968-x.
[8] C. Shen, J. Zhang, J. Ge, Microstructures and electrochemical behaviors of the friction stir welding dissimilar weld, J. Environ. Sci. 23 (2011) S32–S35, https://doi.org/10.1016/S1001-0742(11)61072-3.
[9] T.W. Mendez, F. Patricio, Eagar, welding processes for aeronautics, Adv. Mater. Process. (2001) 39–43.
[10] A.B. Oliviecki, N.J. Beskow, Analysis of the parameters of friction welding process of an aluminum alloy, Perspectiva 37 (2013) 15–29, https://doi.org/10.2166/wp.2013.010.

[11] R. Zettler, A.A.M. da Silva, S. Rodrigues, A. Blanco, J.F. dos Santos, Dissimilar Al to Mg alloy friction stir welds, Adv. Eng. Mater. 8 (2006) 415–421, https://doi.org/10.1002/adem.200600030.
[12] D. Sidane, E. Bousquet, O. Devos, M. Puiggali, M. Touzet, V. Vivier, A. Poulon-Quintin, Local electrochemical study of friction stir welded aluminum alloy assembly, J. Electroanal. Chem. 737 (2015) 206–211, https://doi.org/10.1016/j.jelechem.2014.06.025.
[13] G. Wang, Y. Zhao, Y. Hao, Friction stir welding of high-strength aerospace aluminum alloy and application in rocket tank manufacturing, J. Mater. Sci. Technol. 34 (2018) 73–91, https://doi.org/10.1016/j.jmst.2017.11.041.
[14] R.S. Mishra, Z.Y. Ma, Friction stir welding and processing, Mater. Sci. Eng. R Reports. 50 (2005) 1–78, https://doi.org/10.1016/j.mser.2005.07.001.
[15] https://www.theguardian.com/business/2006/feb/23/theairlineindustry.travelnews (Accessed May 2, 2018).
[16] http://www.aeronewstv.com/en/lifestyle/in-your-opinion/2782-a-boeing-747-8-has-how-many-rivets.html (Accessed May 2, 2018).
[17] E.A. Starke, J.T. Staley, Application of modern aluminium alloys to aircraft. A volume in woodhead publishing series in metal and surface engineering, Fundam. Alum. Metall. Prod. Process. Appl. (2011) 747–783.
[18] C.C. Rusu, L.R. Mistodie, Thermography used in friction stir welding processes, Ann. "Dunarea Jos" Univ. Galati, Fascicle XII, Weld. Equip. Technol. 21 (2010), pp. 1–78, https://doi.org/10.1016/j.mser.2005.07.001.
[19] P.L. Threadgill, Terminology in friction stir welding, Sci. Technol. Weld. Join. 12 (2007) 357–360, https://doi.org/10.1179/174329307X197629.
[20] M.X. Milagre, N.V. Mogili, U. Donatus, R.A.R. Giorjão, M. Terada, J.V.S. Araujo, C.S.C. Machado, I. Costa, On the microstructure characterization of the AA2098-T351 alloy welded by FSW, Mater. Charact. 140 (2018) 233–246, https://doi.org/10.1016/j.matchar.2018.04.015.
[21] C. Sharma, D.K. Dwivedi, P. Kumar, Influences of friction stir welding on the microstructure, mechanical and corrosion behaviour of Al-Zn-Mg aluminium alloy 7039, Eng. Rev. 35 (2015) 267–274.
[22] C. Sharma, D.K. Dwivedi, P. Kumar, Friction stir welding of Al- Zn- Mg alloy AA7039, Light Met. 2012, Springer International Publishing, Cham, 2012, pp. 503–507, https://doi.org/10.1007/978-3-319-48179-1_85.
[23] Y.E. Ma, Z.Q. Zhao, Investigation on the corrosion effect of friction stir welded AA2024 T3 aluminum alloy joints, Key Eng. Mater. 525–526 (2012) 129–132, https://doi.org/10.4028/www.scientific.net/KEM.525-526.129.
[24] E. Bousquet, A. Poulon-Quintin, M. Puiggali, O. Devos, M. Touzet, Relationship between microstructure, microhardness and corrosion sensitivity of an AA 2024-T3 friction stir welded joint, Corros. Sci. 53 (2011) 3026–3034, https://doi.org/10.1016/j.corsci.2011.05.049.
[25] Y.S. Sato, H. Kokawa, S. Kurihara, Systematic examination of precipitation phenomena associated with hardness and corrosion properties in friction stir welded aluminium alloy 2024, Weld. World. 55 (2011) 39–47, https://doi.org/10.1007/BF03321541.
[26] U. Donatus, B.V.G. de Viveiros, M.C. de Alencar, R.O. Ferreira, M.X. Milagre, I. Costa, Correlation between corrosion resistance, anodic hydrogen evolution and microhardness in friction stir weldment of AA2198 alloy, Mater. Charact. 144 (2018) 99–112, https://doi.org/10.1016/j.matchar.2018.07.004.
[27] V. Proton, J. Alexis, E. Andrieu, C. Blanc, J. Delfosse, L. Lacroix, G. Odemer, Influence of post-welding heat treatment on the corrosion behavior of a 2050-T3 aluminum-copper-lithium alloy friction stir welding joint, J. Electrochem. Soc. 158 (2011) C139, https://doi.org/10.1149/1.3562206.
[28] E.A. Starke, J.T. Staley, Application of modern aluminum alloys to aircraft, Prog. Aerosp. Sci. 32 (1996) 131–172, https://doi.org/10.1016/0376-0421(95)00004-6.
[29] H.S. Patil, S.N. Soman, Effect of weld parameter on mechanical and metallurgical properties of dissimilar joints AA6082–AA6061 in T6 condition produced by FSW, Frat. Ed Integrità Strutt. 7 (2013) 151–160, https://doi.org/10.3221/IGF-ESIS.24.16.
[30] A. Davoodi, Z. Esfahani, M. Sarvghad, Microstructure and corrosion characterization of the interfacial region in dissimilar friction stir welded AA5083 to AA7023, Corros. Sci. 107 (2016) 133–144, https://doi.org/10.1016/j.corsci.2016.02.027.
[31] P. Wu, Y. Deng, S. Fan, H. Ji, X. Zhang, A study on dissimilar friction stir welded between the Al–Li–Cu and the Al–Zn–Mg–Cu alloys, Materials (Basel) 11 (2018) 1132, https://doi.org/10.3390/ma11071132.
[32] D. Zhang, Corrosion behavior study of aluminum alloy 7075-T6 and 2A12-T6 joints prepared using friction stir welding, Int. J. Electrochem. Sci. (2020) 1072–1081, https://doi.org/10.20964/2020.02.03.
[33] F.M. Queiroz, U. Donatus, O.M. Prada Ramirez, J.V. de Sousa Araujo, B.V. Gonçalves de Viveiros, S. Lamaka, M. Zheludkevich, M. Masoumi, V. Vivier, I. Costa, H. Gomes de Melo, Effect of unequal levels of deformation and fragmentation on the electrochemical response of friction stir welded AA2024-T3 alloy, Electrochim. Acta. 313 (2019) 271–281, https://doi.org/10.1016/j.electacta.2019.04.137.
[34] C. Zhang, Y. Cao, G. Huang, Q. Zeng, Y. Zhu, X. Huang, N. Li, Q. Liu, Influence of tool rotational speed on local microstructure, mechanical and corrosion behavior of dissimilar AA2024/7075 joints fabricated by friction stir welding, J. Manuf. Process. 49 (2020) 214–226, https://doi.org/10.1016/j.jmapro.2019.11.031.
[35] C.P. De Abreu, Caracterização da reatividade das ligas alumínio AA2024-T3 e AA7475-T651 soldadas por fricção (FSW), Universidade de São Paulo, 2016 in Portuguese.
[36] Tde A. Coutinho, Metalografia de Não - Ferrosos, (1980) in Portuguese.
[37] A.S. Fioravanti, Soldagem por FSW de ligas de alumínio Alclad AA2024-T3 e AA7075-T6, Universidade Federal do Rio Grande do Sul, 2008, https://doi.org/10.1017/CBO9781107415324.004 in Portuguese.
[38] N. Birbilis, M.K. Cavanaugh, R.G. Buchheit, Electrochemical behavior and localized corrosion associated with Al7Cu2Fe particles in aluminum alloy 7075-T651, Corros. Sci. 48 (2006) 4202–4215, https://doi.org/10.1016/j.corsci.2006.02.007.
[39] R.G. Buchheit, Local dissolution phenomena associated with S phase (Al[sub 2]CuMg) particles in aluminum alloy 2024-T3, J. Electrochem. Soc. 144 (1997) 2621, https://doi.org/10.1149/1.1837874.
[40] F.M. Queiroz, M. Magnani, I. Costa, H.G. de Melo, Investigation of the corrosion behaviour of AA 2024-T3 in low concentrated chloride media, Corros. Sci. 50 (2008) 2646–2657, https://doi.org/10.1016/j.corsci.2008.06.041.
[41] A. Boag, A.E. Hughes, A.M. Glenn, T.H. Muster, D. McCulloch, Corrosion of AA2024-T3 part I: localised corrosion of isolated IM particles, Corros. Sci. 53 (2011) 17–26, https://doi.org/10.1016/j.corsci.2010.09.009.
[42] A.E. Hughes, A. Boag, A.M. Glenn, D. McCulloch, T.H. Muster, C. Ryan, C. Luo, X. Zhou, G.E. Thompson, Corrosion of AA2024-T3 part II: co-operative corrosion, Corros. Sci. 53 (2011) 27–39, https://doi.org/10.1016/j.corsci.2010.09.030.
[43] W.-J. Lee, S.-I. Pyun, Effects of sulphate ion additives on the pitting corrosion of pure aluminium in 0.01 M NaCl solution, Electrochim. Acta. 45 (2000) 1901–1910, https://doi.org/10.1016/S0013-4686(99)00418-1.
[44] F. Mansfeld, J.C.S. Fernandes, Impedance spectra for aluminum 7075 during the early stages of immersion in sodium chloride, Corros. Sci. 34 (1993) 2105–2108, https://doi.org/10.1016/0010-938X(93)90063-M.
[45] M.W. Mahoney, C.G. Rhodes, J.G. Flintoff, W.H. Bingel, R.A. Spurling, Properties of friction-stir-welded 7075 T651 aluminum, Metall. Mater. Trans. A 29 (1998) 1955–1964, https://doi.org/10.1007/s11661-998-0021-5.
[46] D.A. Wadeson, X. Zhou, G.E. Thompson, P. Skeldon, L.D. Oosterkamp, G. Scamans, Corrosion behaviour of friction stir welded AA7108 T79 aluminium alloy, Corros. Sci. 48 (2006) 887–897, https://doi.org/10.1016/j.corsci.2005.02.020.
[47] C. Sharma, D.K. Dwivedi, P. Kumar, Influences of friction stir welding on the microstructure, mechanical and corrosion behaviour of Al-Zn-Mg aluminium alloy 7039, Eng. Rev. 35 (2015) 267–274.